

---

# DEEP INVERTIBLE AUTOENCODERS FOR DIMENSIONALITY REDUCTION OF DYNAMICAL SYSTEMS

---

Nicolò Botteghi<sup>1,\*</sup>, Silke Glas<sup>2</sup>, and Christoph Brune<sup>2</sup>

<sup>1</sup>MOX Laboratory, Department of Mathematics, Politecnico di Milano, Milano, Italy

<sup>2</sup>Department of Applied Mathematics, University of Twente, Enschede, Netherlands

\*Corresponding author, nicolo.botteghi@polimi.it

## ABSTRACT

Constructing reduced-order models (ROMs) capable of efficiently predicting the evolution of high-dimensional, parametric systems is crucial in many applications in engineering and applied sciences. A popular class of projection-based ROMs projects the high-dimensional full-order model (FOM) dynamics onto a low-dimensional manifold. These projection-based ROMs approaches often rely on classical model reduction techniques such as proper orthogonal decomposition (POD) or, more recently, on neural network architectures such as autoencoders (AEs). In the case that the ROM is constructed by the POD, one has approximation guaranteed based on the singular values of the problem at hand. However, POD-based techniques can suffer from slow decay of the singular values in transport- and advection-dominated problems. In contrast to that, AEs allow for better reduction capabilities than the POD, often with the first few modes, but at the price of theoretical considerations. In addition, it is often observed, that AEs exhibits a plateau of the projection error with the increment of the dimension of the trial manifold.

In this work, we propose a deep invertible AE architecture, named *inv-AE*, that improves upon the stagnation of the projection error typical of traditional AE architectures, e.g., convolutional, and the reconstructions quality. Inv-AE is composed of several invertible neural network layers that allows for gradually recovering more information about the FOM solutions the more we increase the dimension of the reduced manifold. Through the application of inv-AE to a parametric 1-dimensional Burgers' equation and a parametric 2-dimensional fluid flow around an obstacle with variable geometry, we show that (i) inv-AE mitigates the issue of the characteristic plateau of (convolutional) AEs and (ii) inv-AE can be combined with popular projection-based ROM approaches, e.g., DL-ROM and POD-DL-ROM, to improve their accuracy.

**Keywords** Model-order Reduction · Deep Invertible Autoencoder · Nonlinear Dimensionality Reduction

## 1 Introduction

Many applications in engineering and applied science, e.g., fluid dynamics, chemical and process engineering, climate science, and (soft) robotics, require accurate physical modeling of the systems by means of partial differential equations (PDEs). Often, these systems do not yield closed-form solutions such that numerical simulations are needed to provide approximations. Usually, the solution of these high-dimensional models, which we refer to as full-order models (FOMs), is often computational demanding, limiting the application of such models in all the scenarios requiring real-time or iterative integration, e.g., in optimal control, reinforcement learning, or uncertainty quantification [1]. Reducing the computational cost of the FOMs by investigating new strategies for efficient model reduction (MOR) has been a research focus for decades and, more recently, the advances of machine learning had a significant influence on the development of data-driven reduced-order models (ROMs).

In case that the underlying equations are available, one popular option for building ROMs is by projection of the FOM equations onto a trial manifold, see, e.g., [1, 2, 3, 4, 5]. The trial manifold can be obtained using linear or nonlinear projection-based techniques such as proper orthogonal decomposition (POD) or autoencoders (AE) [6]. While

linear projection techniques based on the singular value decomposition (SVD) have solid mathematical foundations and implementations, they may suffer from slow decay of the singular values in transport- and advection-dominated problems [7]. The slow decay of the singular values negatively affects the reduction capabilities of the linear-subspace ROMs, making the dimension of the trial manifold extremely large, if high accuracy is required, and thus might not allow a drastic reduction of the computational cost of the ROM compared to the FOM. This is due to the fact, that linear-subspace ROMs have a lower bound for the approximation quality, the so-called Kolmogorov  $n$ -widths. The Kolmogorov  $n$ -widths denote the best-possible error for a linear-subspace projection-based ROM of size  $n$ , however, in most cases, there is no explicit construction available how this best-possible approximation error can be attained.

The recent advances of machine learning have made nonlinear projection-based techniques, such as AEs, more and more appealing. AE-based methods can improve the reduction capabilities of linear-subspace MOR methods in challenging problems, showing better decay of the approximation errors, especially within the first few eigenfunctions [8, 9, 10, 5, 11, 12]. However, the use of neural networks (NNs) often complicated theoretical consideration of the approximation bounds of the techniques. Additionally, as observed in e.g., [13, 14, 15], the projection error of AEs, namely the error due to the reduction of dimensionality, with respect to the dimension of the trial manifold, exhibits a plateau (often in the order of  $10^{-3}$ ) after approximately reaching the intrinsic dimension of the underlying problem. This critical drawback of AE architecture poses a strict lower bound on the approximation capabilities of the resulting ROMs.

AEs utilize two NNs to approximate the projection mappings that are commonly referred to in the machine learning community as the *encoder* and the *decoder*. However, the encoder is (usually) a non-invertible function that does not allow the decoder to properly recover the inputs accurately. The non-invertibility of the encoder makes the decoder process ambiguous and causes loss of information [16]. Increasing the latent dimension does not mitigate this drawback and it explains the plateau observed in [13] when AEs are used for building ROMs. Building symmetric AEs by construction has been shown by, e.g., [17, 18] to be an effective strategy to improve upon traditional AE architectures in terms of performance and theoretical guarantees. However, the construction of such symmetric AEs comes at the price of relying on specialized cost functions or additional computational complexity.

The construction of *analytically invertible* NNs layers, such as coupling layers, invertible residual networks, and Glow-type layers [19, 20, 21, 22, 23, 24] has gained attention due to the numerous methods and applications that can benefit from them, e.g., generative models, density estimation, normalizing flows, generative adversarial [25, 26, 27, 28, 29], bi-directional training and efficient backpropagation [21], inverse problems [30, 31], fundamental analysis [32, 33, 34, 35], and, recently, dimensionality reduction with autoencoders [16, 36, 37]. However, it is worth mentioning that the analytical invertibility of invertible NNs do not necessarily translates into their *numerical invertibility*. As highlighted in [35], invertible NNs often experience exploding inverses due to numerical instabilities and errors. The Lipschitz constant of the invertible NNs determines how much these errors are magnified or attenuated. Therefore, controlling the Lipschitz constant is crucial for the numerical stability and invertibility of invertible NNs. Different invertible NN layers have different stability properties, but in general numerical errors become more severe the more we increase the depth of the models. Spectral normalization [38], sigmoid scaling [29], and weight initialization [39] can be used to control the local stability of the invertible NNs. However, global stability of the forward and backward pass is often hard to guarantee [35].

In this work, we focus on enhancing nonlinear projection-based ROMs. In particular, we propose an analytically and numerically invertible AE (*inv-AE*) architecture, tailored to MOR, that overcomes the projection error plateau characterizing traditional AE architectures composed of feedforward or convolutional NN layers. To construct an inv-AE, we stack multiple *invertible affine coupling layers* [19, 20] to build an invertible NN. The forward pass through the invertible NN represents the encoder  $\phi$ , while the backward pass represents the decoder  $\psi$  that in this case is equal to the inverse of the encoder by construction, i.e.,  $\psi = \phi^{-1}$  (restricted to its image). In this way, through *parameter sharing* of encoder and decoder, we are capable of drastically reducing the number of learnable parameters and consequently the training cost. With reference to Figure 1, a generic snapshot  $x_k^\mu$  is projected by the invertible layers, with learnable parameters  $\theta_\phi$ , to  $\phi(x_k^\mu; \theta_\phi)$ . An invertible NN requires the inputs to be of the same dimension of its outputs. Thus, to reduce the dimensionality and promote the compression of information onto a lower-dimensional manifold, we zero-mask  $\phi(x_k^\mu; \theta_\phi)$  up to the chosen latent dimensionality to obtain  $z_k^\mu$ . After zero-masking,  $z_k^\mu$  is used fed to the inverse mapping  $\phi^{-1}(z_k^\mu; \theta_\phi)$ , i.e., the decoder of traditional AEs, to recover the reconstruction  $\hat{x}_k^\mu$  of  $x_k^\mu$ . With this simple zero-masking, inspired by [16], we have transformed an invertible NN into an inv-AE.

In many complex problems, such as in fluid dynamics, the snapshots can be extremely high-dimensional. However, it is possible to first perform dimensionality-reduction using SVD on the data matrix

$$\mathbf{X}_{\text{train}} \approx \mathbf{U}\mathbf{\Sigma}\mathbf{V}^\top,$$

where  $\mathbf{U} \in \mathbb{R}^{N \times r}$ ,  $\mathbf{\Sigma} \in \mathbb{R}^{r \times r}$ ,  $\mathbf{V} \in \mathbb{R}^{(N_t \times |\mathcal{P}_{\text{train}}|) \times r}$ , with  $r$  being the chosen number of modes used to represent the data. Using  $\mathbf{U}^\top$  we can obtain the POD coefficient  $h_k^\mu$  from  $x_k^\mu$  and rely on the inv-AE to recover the POD coefficients

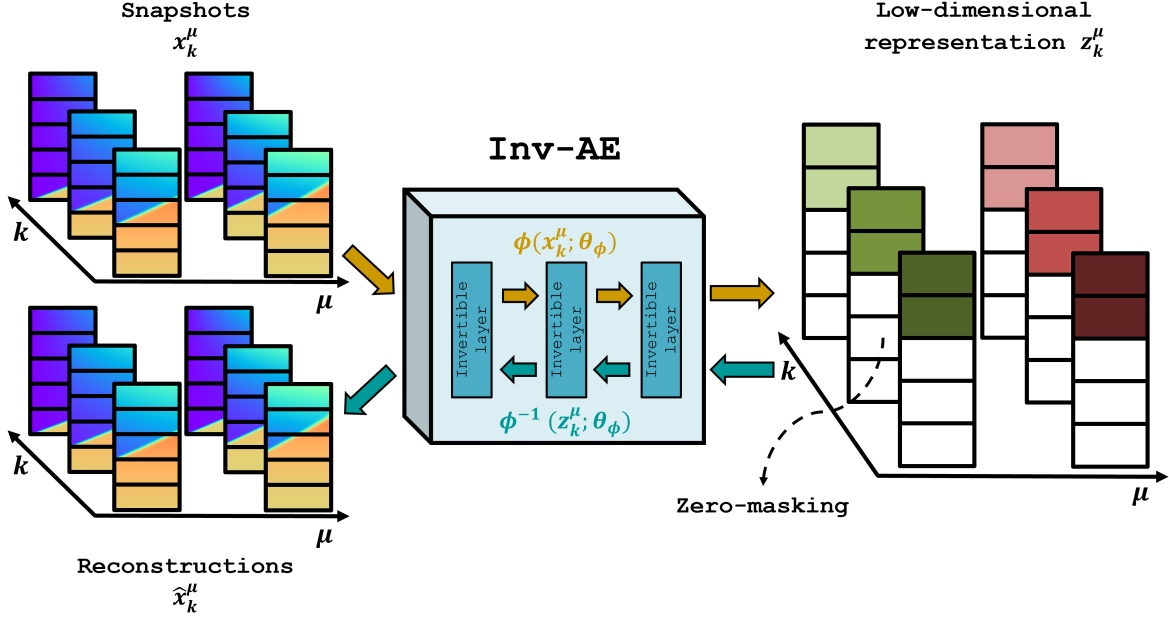


Figure 1: Dimensionality reduction with inv-AE. The snapshots  $x_k^\mu$  are encoded using the encoder  $\phi(x_k^\mu; \theta_\phi)$ , successively zero-masked up to a chosen latent dimension, and eventually decoded using the inverse of the encoder  $\phi^{-1}(z_k^\mu; \theta_\phi)$ .

$h_k^\mu$ . Eventually, using  $U$  we can recover the reconstruction  $\hat{x}_k^\mu$  of  $x_k^\mu$  from the reconstructed POD coefficients  $\hat{h}_k^\mu$ . We refer to this approach as *POD-inv-AE* and we depict it in Figure 2.

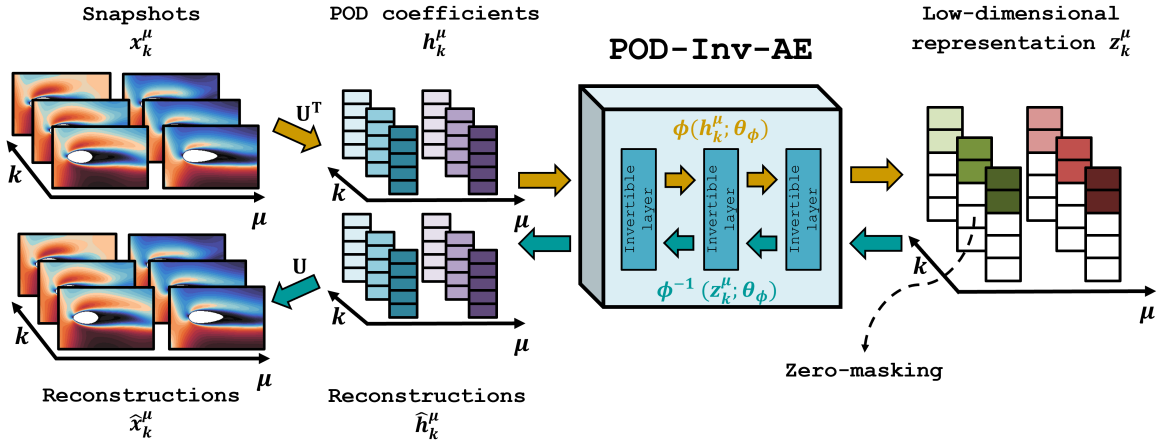


Figure 2: Dimensionality reduction with POD-inv-AE. The snapshots dimensionality is first reduced using POD, then the POD coefficients are further compressed by zero-masking output of encoder  $\phi(x_k^\mu; \theta_\phi)$ . The POD coefficients are recovered by decoding the latent variables  $\phi^{-1}(z_k^\mu; \theta_\phi)$ , and eventually the snapshots are reconstructed from the POD coefficients using  $U$ .

We numerically study the reduction capabilities of inv-AE and POD-inv-AE on a parametric Burgers' equation, analogously to [13], and on a parametric fluid flow around a obstacle with variable geometry. Eventually, we show that inv-AE and POD-inv-AE can replace the traditional AE architectures of popular deep learning-based ROM techniques such as DL-ROM [5] and POD-DL-ROM [40] to improve the accuracy of the predictions and consequently the performance of the resulting ROMs.

The rest of the paper is organized as follows: Section 2 introduces problem settings, linear and nonlinear strategies for dimensionality reduction, and deep learning-based ROM. Section 3 presents the proposed invertible AE architecture

and its combination with deep learning-based ROM. Section 4 shows the numerical experiments, results, and discusses the findings. Eventually, Section 5 concludes the paper.

## 2 Preliminaries

In this section, we summarize existing background knowledge needed for further comprehension of the paper. We begin by stating the parametric initial value problem, its MOR, the limitations of linear-subspace MOR, and AEs in Section 2.1. Further, in Section 2.2 we introduce (POD) DL-ROMs based on AEs.

### 2.1 Problem Setting and Limitations of Linear-subspace Model Reduction

We consider parametric initial value problems as our FOM model: for given  $\boldsymbol{\mu} \in \mathcal{P} \subset \mathbb{R}^p, p \in \mathbb{N}$  and initial condition  $\boldsymbol{x}_0(\boldsymbol{\mu}) \in \mathbb{R}^N$ , we seek the solution  $\boldsymbol{x}(\cdot; \boldsymbol{\mu}) \in C^1(\mathcal{I}; \mathbb{R}^N)$  such that

$$\frac{d}{dt} \boldsymbol{x}(t; \boldsymbol{\mu}) = \boldsymbol{f}(t, \boldsymbol{x}(t; \boldsymbol{\mu}); \boldsymbol{\mu}), \quad \boldsymbol{x}(t_0; \boldsymbol{\mu}) = \boldsymbol{x}_0(\boldsymbol{\mu}) \in \mathbb{R}^N, \quad (1)$$

using time interval  $\mathcal{I} = (t_0, t_f]$  and  $t_0 < t_f < \infty$ , and right-hand side  $\boldsymbol{f} : \mathcal{I} \times \mathbb{R}^N \times \mathcal{P} \rightarrow \mathbb{R}^N$ . By solving the FOM with a numerical integration scheme in time, we obtain a collection of snapshots of the type  $\boldsymbol{x}(t; \boldsymbol{\mu}) \rightarrow \boldsymbol{x}(t_k; \boldsymbol{\mu}) = \boldsymbol{x}_k^\mu$  for  $k = 1, \dots, N_t$  for each parameter  $\boldsymbol{\mu}$  in a discrete training set  $\mathcal{P}_{\text{train}} \subseteq \mathcal{P}$ . The collection of snapshots compose our data matrix such that we arrive at

$$\boldsymbol{X}_{\text{train}} = \left[ \begin{array}{c|c|c|c|c} \boldsymbol{x}_1^{\mu_1} & \boldsymbol{x}_2^{\mu_1} & \cdots & \boldsymbol{x}_{N_t-1}^{\mu_{|\mathcal{P}_{\text{train}}|}} & \boldsymbol{x}_{N_t}^{\mu_{|\mathcal{P}_{\text{train}}|}} \\ \hline \boldsymbol{x}_1^{\mu_1} & \boldsymbol{x}_2^{\mu_1} & \cdots & \boldsymbol{x}_{N_t-1}^{\mu_{|\mathcal{P}_{\text{train}}|}} & \boldsymbol{x}_{N_t}^{\mu_{|\mathcal{P}_{\text{train}}|}} \\ \hline \boldsymbol{x}_1^{\mu_1} & \boldsymbol{x}_2^{\mu_1} & \cdots & \boldsymbol{x}_{N_t-1}^{\mu_{|\mathcal{P}_{\text{train}}|}} & \boldsymbol{x}_{N_t}^{\mu_{|\mathcal{P}_{\text{train}}|}} \\ \hline \boldsymbol{x}_1^{\mu_1} & \boldsymbol{x}_2^{\mu_1} & \cdots & \boldsymbol{x}_{N_t-1}^{\mu_{|\mathcal{P}_{\text{train}}|}} & \boldsymbol{x}_{N_t}^{\mu_{|\mathcal{P}_{\text{train}}|}} \end{array} \right] \in \mathbb{R}^{N \times (N_t \times |\mathcal{P}_{\text{train}}|)}.$$

Given the FOM in (1), a ROM can be constructed via projection with the two mappings previously denoted as encoder  $\phi : \mathbb{R}^N \rightarrow \mathbb{R}^n$  and decoder  $\psi : \mathbb{R}^n \rightarrow \mathbb{R}^N$  such that  $\phi \circ \psi = \text{id}_{\mathbb{R}^n}$  and  $n \ll N$ . Two terms commonly used in MOR are the computational intense offline phase, which is dependent on the FOM dimension  $N$  and in which the ROM is built, as well as the cost-effective online phase, where the ROM (ideally only depending on the latent dimension  $n$ ) is evaluated. Linear-subspace MOR methods employs linear mappings for  $\phi$  and  $\psi$ , while in the case of MOR on manifolds, the mappings  $\phi$  and  $\psi$  are nonlinear functions.<sup>1</sup> Particularly, we use the Manifold Galerkin projection, which was introduced in [13], resulting in the following ROM: for given  $\boldsymbol{\mu} \in \mathcal{P} \subset \mathbb{R}^p, p \in \mathbb{N}$  and  $\tilde{\boldsymbol{x}}_0(\boldsymbol{\mu})$  we seek  $\tilde{\boldsymbol{x}}(\cdot; \boldsymbol{\mu}) \in C^1(\mathcal{I}; \mathbb{R}^n)$  such that

$$\frac{d}{dt} \tilde{\boldsymbol{x}}(t; \boldsymbol{\mu}) = (\boldsymbol{D}\psi(\tilde{\boldsymbol{x}}(t; \boldsymbol{\mu}))^\dagger \boldsymbol{f}(t, \psi(\tilde{\boldsymbol{x}}(t; \boldsymbol{\mu})); \boldsymbol{\mu}), \quad \tilde{\boldsymbol{x}}(t_0; \boldsymbol{\mu}) = \phi(\boldsymbol{x}_0(\boldsymbol{\mu})) \in \mathbb{R}^n,$$

where  $(\boldsymbol{D}\psi(\tilde{\boldsymbol{x}}(t; \boldsymbol{\mu})))^\dagger$  denotes the Moore-Penrose pseudo-inverse of the Jacobian of  $\psi$  evaluated at the reduced state  $\tilde{\boldsymbol{x}}(t; \boldsymbol{\mu})$ .

In the case, that the mapping  $\phi, \psi$  are linear the quality of the resulting ROM approximation can be bounded from below by the Kolmogorov  $n$ -widths. In many applications, such as in elliptic and parabolic partial differential equations, see, e.g., [42, 43], it is observed, that Kolmogorov  $n$ -widths can obtain an exponential decay. However, in the case of transport-dominated problems, the Kolmogorov  $n$ -widths may decay slowly [7]. One possibility on how to break this Kolmogorov barrier is to employ nonlinear mapping for  $\phi, \psi$  such as autoencoders.

AEs [44, 6] are special types of NN architectures used for dimensionality reduction. An AE (i) maps the high-dimensional data onto a low-dimensional latent variable representation using the encoder and (ii) maps the low-dimensional latent variables back to the original high-dimensional data space using the decoder, i.e.,  $\boldsymbol{x} \approx \hat{\boldsymbol{x}} = \psi(\phi(\boldsymbol{x}; \boldsymbol{\theta}_\phi); \boldsymbol{\theta}_\psi)$ . We denote the learnable parameters, namely weights and biases, of the encoder and decoder by  $\boldsymbol{\theta}_\phi$  and  $\boldsymbol{\theta}_\psi$ , respectively. These learnable parameters  $\boldsymbol{\theta}_\phi, \boldsymbol{\theta}_\psi$  of the AE are jointly optimized by minimizing the reconstruction loss over a (train) set  $X$  on  $M$  training samples that we indicate as  $\{\boldsymbol{x}^{(1)}, \dots, \boldsymbol{x}^{(M)}\}$ , i.e.,

$$\mathcal{L}(\boldsymbol{\theta}_\phi, \boldsymbol{\theta}_\psi) = \frac{1}{M} \sum_{i=1}^M \|\boldsymbol{x}^{(i)} - \hat{\boldsymbol{x}}^{(i)}\|_2^2 = \frac{1}{M} \sum_{i=1}^M \|\boldsymbol{x}^{(i)} - \psi(\phi(\boldsymbol{x}^{(i)}; \boldsymbol{\theta}_\phi); \boldsymbol{\theta}_\psi)\|_2^2, \quad (2)$$

where  $\boldsymbol{x}^{(i)}$  indicates the  $i^{\text{th}}$  training data and  $\hat{\boldsymbol{x}}^{(i)}$  its reconstruction using the AE. The dimension of the latent space is a hyper-parameter of the AE model that can be chosen using prior knowledge or through a trail-and-error approach. Moreover, for  $\psi, \phi$  being nonlinear mappings, adjusted variants of limiting widths can be investigated, where we refer the interested reader to [45] for an overview of nonlinear widths.

<sup>1</sup>For a general differential geometric formulation of MOR on manifolds, we refer the reader to [41].

## 2.2 (POD) Deep Learning-based ROMs

The method of Deep Learning-based ROM (DL-ROM) [5] is a popular and effective approach for learning ROMs from data. In this context, the generic  $i^{\text{th}}$  data  $\mathbf{x}^{(i)}$  corresponds to the  $i^{\text{th}}$  FOM snapshot  $\mathbf{x}_k^\mu$  that might have temporal and parametric dependencies. DL-ROM is composed of a (convolutional) encoder  $\phi(\mathbf{x}_k^\mu; \boldsymbol{\theta}_\phi)$  and a (convolutional) decoder  $\psi(\mathbf{z}_k^\mu; \boldsymbol{\theta}_\psi)$  that learn a low-dimensional representation  $\mathbf{z}_k^\mu$  of the snapshots and their reconstructions  $\tilde{\mathbf{x}}_k^\mu$  in parallel. To efficiently predict the system's dynamics, DL-ROM uses a feedforward NN  $\boldsymbol{\xi}(\boldsymbol{\mu}, t; \boldsymbol{\theta}_\xi)$ , with learnable parameters  $\boldsymbol{\theta}_\xi$ , to predict the latent snapshot  $\tilde{\mathbf{z}}_k^\mu$  from the timestep  $t$  and parameter vector  $\boldsymbol{\mu}$ . We can then retrieve the approximated FOM snapshots by decoding  $\tilde{\mathbf{z}}_k^\mu$ . We can optimize the DL-ROM parameters, namely  $\boldsymbol{\theta}_\phi$ ,  $\boldsymbol{\theta}_\psi$ , and  $\boldsymbol{\theta}_\xi$ , by minimizing over the loss function

$$\begin{aligned} \mathcal{L}_{\text{DL-ROM}}(\boldsymbol{\theta}_\phi, \boldsymbol{\theta}_\psi, \boldsymbol{\theta}_\xi) &= \frac{1}{M} \sum_{i=1}^M \left( \frac{\alpha}{2} \|\mathbf{x}^{(i)} - \tilde{\mathbf{x}}^{(i)}\|_2^2 + \frac{1-\alpha}{2} \|\mathbf{z}^{(i)} - \tilde{\mathbf{z}}^{(i)}\|_2^2 \right) \\ &= \frac{1}{M} \sum_{i=1}^M \left( \frac{\alpha}{2} \|\mathbf{x}^{(i)} - \psi(\tilde{\mathbf{z}}^{(i)}; \boldsymbol{\theta}_\psi)\|_2^2 + \frac{1-\alpha}{2} \|\phi(\mathbf{x}^{(i)}; \boldsymbol{\theta}_\phi) - \tilde{\mathbf{z}}^{(i)}\|_2^2 \right) \\ &= \frac{1}{M} \sum_{i=1}^M \left( \frac{\alpha}{2} \|\mathbf{x}^{(i)} - \psi(\boldsymbol{\xi}(t^{(i)}, \boldsymbol{\mu}^{(i)}; \boldsymbol{\theta}_\xi); \boldsymbol{\theta}_\psi)\|_2^2 + \frac{1-\alpha}{2} \|\phi(\mathbf{x}^{(i)}; \boldsymbol{\theta}_\phi) - \boldsymbol{\xi}(t^{(i)}, \boldsymbol{\mu}^{(i)}; \boldsymbol{\theta}_\xi)\|_2^2 \right), \end{aligned} \quad (3)$$

where  $0 \leq \alpha \leq 1$ . In the online phase, we use  $\boldsymbol{\xi}(t, \boldsymbol{\mu}; \boldsymbol{\theta}_\xi)$  to predict the evolution of the system at an arbitrary timestep  $t$  for a given  $\boldsymbol{\mu}$  and decode the latent snapshots using the decoder to retrieve approximations to the FOM solutions.

The POD-DL-ROM method [40] extends DL-ROM with an additional POD reduction step before the AE neural network to drastically reducing the number of learnable parameters of the AE and consequently reduce the training times. First the POD is computed for a chosen dimension  $r$ ,  $n \leq r \leq N$ . Using the POD basis  $\mathbf{U} \in \mathbb{R}^{N \times r}$  the respective POD coefficients  $\mathbf{h}_k^\mu := \mathbf{U}^\top \mathbf{x}_k^\mu$  on the intermediate linear subspace  $\mathbb{R}^r$  are computed. Subsequently, the DL-ROM is trained using (3) by replacing  $\mathbf{x}_k^\mu$  with the POD coefficients  $\mathbf{h}_k^\mu$ . In the online phase, we follow the DL-ROM steps and afterwards recover the FOM solutions from the reconstructed POD coefficients, i.e.,  $\tilde{\mathbf{x}}_k^\mu = \mathbf{U} \tilde{\mathbf{h}}_k^\mu = \mathbf{U} \psi(\boldsymbol{\xi}(t, \boldsymbol{\mu}; \boldsymbol{\theta}_\xi); \boldsymbol{\theta}_\psi)$ . Note, that for the POD-DL-ROM, an adjusted version of the Kolmogorov  $n$ -widths holds, due to the linear reduction step introduced by the POD, see [46].

## 3 Invertible Autoencoders for Dimensionality and Model Reduction

Traditional AE architectures utilize (deep) NNs to parametrize the encoder and decoder and minimize the reconstruction loss (2) to optimize the learnable parameters of the two architectures. However, the encoder is usually non-invertible and, therefore, it cannot be inverted by the decoder, resulting in a loss of information [16]. The loss of information is typically not reduced by increasing the dimension of the manifold, i.e., using more latent variables, and it is correlated with the projection-error plateau firstly observed by [13] in the context of data-driven ROM. To tackle the problem of (non-)invertibility of AE architectures, inspired by [16], we propose an *analytically and numerically invertible AE* (*inv-AE*) architecture capable of going beyond the projection-error plateau of traditional AEs.

The rest of the section is organized as follows: Section 3.1 presents the building blocks of inv-AE, namely the invertible NN layers, while Section 3.2 presents the inv-AEs. Eventually, Section 3.3 introduces a new class of DL-ROMs named invertible (POD) DL-ROMs.

### 3.1 Invertible Neural Networks and Layers

Similarly to invertible NNs, the inv-AE is composed of multiple invertible layers. Inv-AE uses invertible affine coupling layers [19, 20], but other invertible layers can be simply plugged-in without changing the core principles. Each affine coupling layer is composed of four nonlinear learnable functions, scaling and translating the input  $\mathbf{x}$ :

1.  $\mathbf{s}_1 : \mathbb{R}^{N/2} \rightarrow \mathbb{R}^{N/2}$ ,
2.  $\mathbf{s}_2 : \mathbb{R}^{N/2} \rightarrow \mathbb{R}^{N/2}$ ,
3.  $\mathbf{t}_1 : \mathbb{R}^{N/2} \rightarrow \mathbb{R}^{N/2}$ , and
4.  $\mathbf{t}_2 : \mathbb{R}^{N/2} \rightarrow \mathbb{R}^{N/2}$ ,

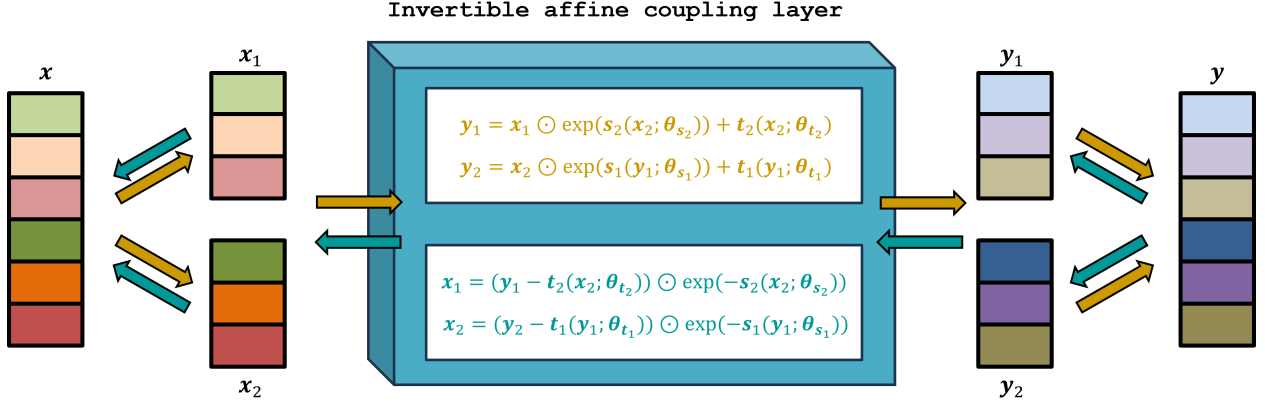


Figure 3: Invertible affine coupling layer. The forward pass through the layer is indicated by dark khaki arrows, while the backward pass by teal arrows.

where  $N$  indicates the dimension of the input  $\mathbf{x}$ . Each function is parametrized by NN with learnable parameter vectors  $\theta_{s_1}, \theta_{s_2}, \theta_{t_1}, \theta_{t_2}$ , respectively. With reference to Figure 3, an affine coupling layer first splits the input  $\mathbf{x}$  of dimension  $N$  in two part of equal dimension, i.e.,  $\mathbf{x}_1, \mathbf{x}_2 \in \mathbb{R}^{N/2}$  such that  $\mathbf{x} = (\mathbf{x}_1, \mathbf{x}_2)^\top$ . Then, the transformations  $s_1(\cdot; \theta_{s_1})$ ,  $s_2(\cdot; \theta_{s_2})$ ,  $t_1(\cdot; \theta_{t_1})$ , and  $t_2(\cdot; \theta_{t_2})$  are applied to  $\mathbf{x}_1$  and  $\mathbf{x}_2$  to obtain the outputs  $\mathbf{y}_1 \in \mathbb{R}^{N/2}$  and  $\mathbf{y}_2 \in \mathbb{R}^{N/2}$  of the layer. The forward pass through an invertible coupling layer can be written by

$$\begin{aligned} \mathbf{y}_1 &= \mathbf{x}_1 \odot \exp(s_2(\mathbf{x}_2; \theta_{s_2})) + t_2(\mathbf{x}_2; \theta_{t_2}) \\ \mathbf{y}_2 &= \mathbf{x}_2 \odot \exp(s_1(\mathbf{y}_1; \theta_{s_1})) + t_1(\mathbf{y}_1; \theta_{t_1}) \end{aligned}$$

where  $\odot$  indicates the Hadamard product and the output  $\mathbf{y}$  is obtained by concatenation of  $\mathbf{y}_1, \mathbf{y}_2$ , i.e.,  $\mathbf{y} = (\mathbf{y}_1, \mathbf{y}_2)^\top \in \mathbb{R}^N$ . The coupling layer is analytically invertible, and we can write its backward pass from  $\mathbf{y}$  to  $\mathbf{x}$  by

$$\begin{aligned} \mathbf{x}_1 &= (\mathbf{y}_1 - t_2(\mathbf{x}_2; \theta_{t_2})) \odot \exp(-s_2(\mathbf{x}_2; \theta_{s_2})) \\ \mathbf{x}_2 &= (\mathbf{y}_2 - t_1(\mathbf{y}_1; \theta_{t_1})) \odot \exp(-s_1(\mathbf{y}_1; \theta_{s_1})) \end{aligned}$$

To prevent numerical instabilities, we clamp and scale the exponential function as proposed in [29]. Therefore, we obtain

$$\begin{aligned} \exp(s_2(\mathbf{x}_2; \theta_{s_2})) &= \exp(\arctan(s_2(\mathbf{x}_2; \theta_{s_2}))) \\ \exp(s_1(\mathbf{y}_1; \theta_{s_1})) &= \exp(\arctan(s_1(\mathbf{y}_1; \theta_{s_1}))) \end{aligned} \quad (4)$$

### 3.2 From Invertible NNs to Invertible AEs

Each invertible layer does not perform any form of dimensionality reduction because to achieve (analytical) invertibility, the layers require the same dimensionality of inputs and outputs, i.e.,  $\mathbf{x}, \mathbf{y} \in \mathbb{R}^N$ . Therefore, using an invertible NN composed of multiple affine coupling layers is not sufficient for building an invertible AE. However, to achieve dimensionality reduction, we use a technique proposed in [16]. We assume  $\mathbf{x}$  to be the input of the first layer and  $\mathbf{y}$  to be the output of the last layer of the invertible NN. In particular, after applying the forward pass transformations, we can mask with zeros the output of the final layer  $\mathbf{y}$  up to an arbitrary latent dimension to obtain  $\mathbf{z}$ :

$$\begin{aligned} \mathbf{y} &= \phi(\mathbf{x}; \theta_\phi) \\ \mathbf{z} &= \text{zero-masking}(\mathbf{y}). \end{aligned} \quad (5)$$

Then, the zero-masked vector  $\mathbf{z}$  is passed through the backward pass to recover the reconstruction of the input  $\hat{\mathbf{x}}$ :

$$\hat{\mathbf{x}} = \psi(\mathbf{z}; \theta_\psi), \quad (6)$$

where  $\psi = \phi^{-1}$  and  $\theta_\psi = \theta_\phi$  (see Figure 1). The zero-masking promotes the compression of the data into a limited number of relevant dimensions, making the invertible NN and inv-AE. Analogously to traditional AEs, we train our inv-AE to minimize the reconstruction loss (2), where encoder and decoder correspond to the forward and backward pass through the invertible layers.

In addition to the reconstruction loss, it is possible to utilize additional terms such a zero-masking regularization loss [16], or a Lipschitz-constant regularization loss [35] to improve numerical stability and convergence properties of the architecture. However, in our case, the choice of an affine coupling layer with clamped exponential (see Equation (4)) is sufficient for preventing numerical instabilities. In addition, we investigate the effect of spectral normalization A on the performance of the inv-AE by spectrally normalizing the NN layers of the architecture. For our numerical experiments, we utilize an inv-AE composed of 5 invertible affine coupling layers. Each of the learnable mappings are parametrized by feedforward NNs composed of one hidden layer with 512 neurons and GeLU activation functions.

### 3.3 Invertible (POD) Deep Learning-based ROMs

In this work, we do not only test the dimensionality-reduction capabilities of the inv-AE, but we also empirically evaluate the advantages of inv-AE in the context of projection-based ROM. Therefore, we propose to enhance the DL-ROM and the POD-DL-ROM (see Section 2.2) with our inv-AE replacing the convolutional AE. We call these two approaches as *inv-DL-ROM* and *POD-inv-DL-ROM*. Analogously to DL-ROM, inv-DL-ROM is composed of an inv-AE and a feedforward NN  $\xi$  predicting the next latent snapshot from the timestep  $k$  and the parameter vector  $\mu$ :

$$\begin{aligned}\tilde{z}_k^\mu &= \xi(k, \mu; \theta_\xi) \\ \tilde{z}_k^\mu &= \text{zero-masking}(\tilde{z}_k^\mu) \\ \tilde{x}_k^\mu &= \psi(\tilde{z}_k^\mu; \theta_\psi),\end{aligned}$$

where  $\psi = \phi^{-1}$  and  $\theta_\psi = \theta_\phi$  and the zero-padding is used to have the dimensionality of  $\tilde{z}_k^\mu$  equal to  $\tilde{x}_k^\mu$  as required by the inv-AE architecture. On the other side, POD-inv-DL-ROM simply adds the POD (re)projection of the POD coefficients to the snapshots:

$$\begin{aligned}\tilde{z}_k^\mu &= \xi(k, \mu; \theta_\xi) \\ \tilde{z}_k^\mu &= \text{zero-masking}(\tilde{z}_k^\mu) \\ \tilde{h}_k^\mu &= \psi(\tilde{z}_k^\mu; \theta_\psi) \\ \tilde{x}_k^\mu &= U\tilde{h}_k^\mu,\end{aligned}$$

where  $U$  is the SVD matrix computed on the train set and  $\tilde{h}_k^\mu$  is the reconstructed POD coefficient using  $\xi$  and  $\psi$ . For the sake of a fair comparison, the learnable parameters of inv-DL-ROM and POD-inv-DL-ROM are optimized using the same objective function of DL-ROM and POD-DL-ROM (see Equation (3)). However, it is worth mentioning that due to the parameter sharing of encoder and decoder, inv-AE reduces the number of learnable parameters of the overall (POD) DL-ROM architecture, addressing the limitation of (POD) DL-ROM that utilizes the encoder only during the offline phase, but not during the online one.

## 4 Numerical Results

To investigate the capabilities on the invertible AEs, we introduce two numerical examples, namely a parametric 1-dimensional Burgers' equation (Section 4.1) and a parametric 2-dimensional fluid flow around an obstacle with variable geometry (Section 4.2). Using these two numerical examples, we aim to test (i) the dimensionality reduction capabilities of inv-AE and POD-inv-AE with respect to a traditional AE and POD-AE with and without spectral normalization (see Appendix A), and (ii) the accuracy of the resulting ROMs, namely inv-DL-ROM and POD-inv-DL-ROM, with respect to DL-ROM and POD-DL-ROM.

After training the models using the train set  $\mathbf{X}_{\text{train}}$ , we evaluate their performance on the test set  $\mathbf{X}_{\text{test}}$

$$\mathbf{X}_{\text{test}} = \begin{bmatrix} | & | & \cdots & | & | \\ \mathbf{x}_1^{\mu_1} & \mathbf{x}_2^{\mu_1} & \cdots & \mathbf{x}_{N_t-1}^{\mu_{\mathcal{P}_{\text{test}}}} & \mathbf{x}_{N_t}^{\mu_{\mathcal{P}_{\text{test}}}} \\ | & | & \cdots & | & | \end{bmatrix} \in \mathbb{R}^{N \times (N_t \times |\mathcal{P}_{\text{test}}|)}.$$

In particular, we utilize the mean projection error given by

$$\frac{1}{|\mathbf{X}_{\text{test}}|} \sum_{\mu \in \mathcal{P}_{\text{test}}} \sqrt{\frac{\sum_{k=1}^{N_t} \|\mathbf{x}_k^\mu - \hat{\mathbf{x}}_k^\mu\|_2^2}{\sum_{k=1}^{N_t} \|\mathbf{x}_k^\mu\|_2^2}}, \quad (7)$$

and the mean reduction error

$$\frac{1}{|\mathbf{X}_{\text{test}}|} \sum_{\mu \in \mathcal{P}_{\text{test}}} \sqrt{\frac{\sum_{k=1}^{N_t} \|\mathbf{x}_k^\mu - \tilde{\mathbf{x}}_k^\mu\|_2^2}{\sum_{k=1}^{N_t} \|\mathbf{x}_k^\mu\|_2^2}}, \quad (8)$$

where  $\mathbf{x}_k^\mu$  indicate the discretized FOM snapshot at the timestep  $k$ ,  $\hat{\mathbf{x}}_k^\mu$  the reconstructed snapshot when passed through encoder and decoder, and  $\tilde{\mathbf{x}}_k^\mu$  the decoded solution of the DL-ROM. The projection error measures the best-possible error made by the corresponding chosen autoencoder realization, while the reduction error shows the error of the corresponding ROM.

#### 4.1 Burgers' Equation

We study a time-dependent 1-dimensional Burgers' equation as introduced in [13] given by

$$\begin{aligned} \frac{\partial x(y, t; \boldsymbol{\mu})}{\partial t} + \frac{\partial f(x(y, t; \boldsymbol{\mu}))}{\partial y} - 0.02 \exp^{\mu_2 y} &= 0, \quad \forall y \in [0, 100], \forall t \in (t_0, t_f], \\ x(0, t; \boldsymbol{\mu}) &= \mu_1, \quad \forall t \in [t_0, t_f], \\ x(y, 0) &= 1, \quad \forall y \in [0, 100], \end{aligned}$$

where the flux is  $f(x) = 0.5x^2$  and  $\boldsymbol{\mu} = (\mu_1, \mu_2)$  is the parameter vector,  $t$  indicates the time variable, and  $y$  the spatial variable. Analogously to [13], we derive the FOM snapshots by numerically solving the Burgers' equation from  $t_0 = 0.0$ , to  $t_f = 35$ , where we use equidistant time steps of  $\Delta t = 0.07s$  resulting in  $N_t = 500$  and discretize in time with the implicit Euler scheme. For the spatial discretization, we apply a Godunov's scheme with  $N = 256$  spatial degrees of freedom. The parameter domain is  $\mathcal{P} = [4.25, 5.5] \times [0.015, 0.03]$ , where we choose a training set of parameters  $\mathcal{P}_{\text{train}}$  by discretizing the parameter intervals into  $10 \times 8 = 80$  bins to replicate [13]. The training set  $X_{\text{train}}$  is composed of the 80 FOM solutions generated for the parameters  $\mathcal{P}_{\text{train}}$ . Further, we keep 8 of the 80 FOM solutions for the validation set  $X_{\text{valid}}$ , while the test set  $X_{\text{test}}$  is composed of 2 FOM solutions generated with 2 unseen parameter values. For the unseen parameter values, we choose the same values as in [13], namely  $\boldsymbol{\mu}_{\text{test}}^{(1)} = (4.3, 0.021)$  and  $\boldsymbol{\mu}_{\text{test}}^{(2)} = (5.15, 0.0285)$ . In this way, we are able to test the generalization capabilities of the proposed AE architectures on unseen instances of the parameter  $\boldsymbol{\mu}$ . We show two examples of Burgers' solution in Figure 4.

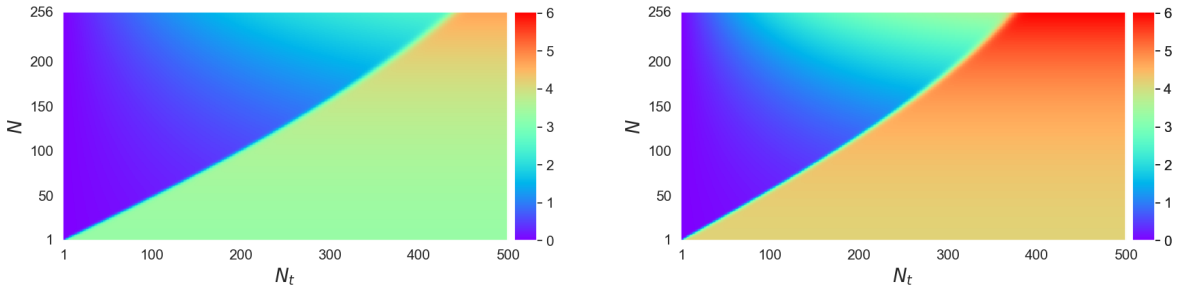


Figure 4: Examples of solution snapshots of the Burgers' equation for the two different instances of the parameter  $\boldsymbol{\mu}_{\text{test}}$ .

In this first experiment, we compare the projection error achieved by our inv-AE and the convolutional AE introduced in [13] for different manifold dimensions  $\in \{1, 2, 3, 4, 5, 10, 20, 50, 100, 150, 200\}$ . In the second experiments, we compare instead the reduction error achieved by inv-DL-ROM with respect to DL-ROM (with the convolution AE of [13]) for different dimensions of the latent space  $\in \{3, 4, 5, 10, 20\}$ . For fairness of the comparison, we train the different models for 1000 epochs with the AdamW optimizer [47]. In addition, we use the same learning rate of  $1e^{-4}$  and weight decay of  $1e^{-4}$ , and we employ early stopping if the loss on the validation set does not decrease after 500 epochs of training. After training the models, we analyze the projection errors achieved by the different AE architectures and the reduction errors achieved by the different DL-ROM architectures.

In Figure 5 we show the projection errors obtained with the different architectures with respect to the chosen dimension of the trial manifold and in Table 1 we report the values. We compare the projection error of the inv-AE with POD and the convolutional AE from [13], where the blue shaded area highlights values up to manifold dimension equal to 50 as reported in [13]. As reported in [13], the convolutional AE exhibits a plateau of the projection error when the dimension of the manifold is 5, while the projection error of our inv-AE with and without spectral normalization continuously decreases with the increment of the manifold dimension and it is consistently smaller than the one of the convolutional AE for a manifold dimension  $> 2$ . The POD has higher projection error than both variants of the AEs for manifold dimensions smaller than 50, while above 100 it outperforms the AEs.

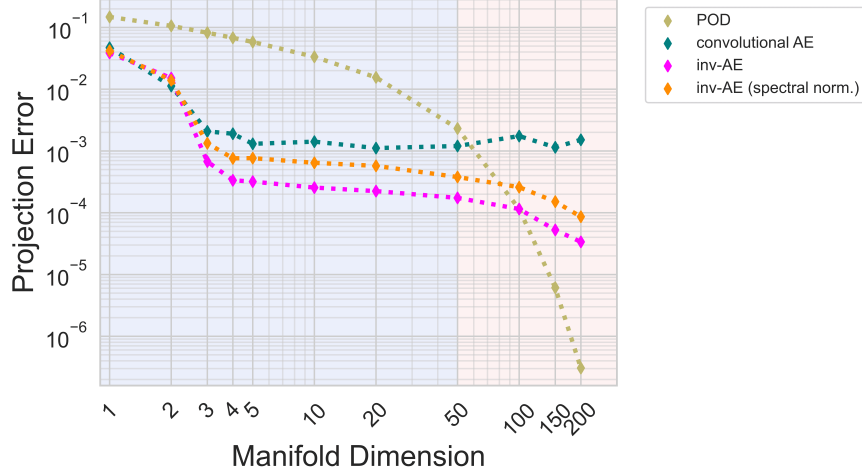


Figure 5: Projection errors (7) calculated on the test set  $X_{\text{test}}$  for different dimensions of the trial manifold.

Manifold Dimension	POD	Convolutional AE	Inv-AE	Inv-AE (spectral norm.)
1	1.48e-1	4.70e-2	<b>3.86e-2</b>	4.19e-2
2	1.06e-1	<b>1.12e-2</b>	1.51e-2	1.40e-2
3	8.20e-2	2.07e-3	<b>6.75e-4</b>	1.34e-3
4	6.79e-2	1.90e-3	<b>3.35e-4</b>	7.59e-4
5	5.81e-2	1.30e-3	<b>3.19e-4</b>	7.65e-4
10	3.34e-2	1.41e-3	<b>2.55e-4</b>	6.43e-4
20	1.55e-2	1.11e-3	<b>2.24e-4</b>	5.73e-4
50	2.31e-3	1.20e-3	<b>1.74e-4</b>	3.78e-4
100	<b>1.15e-4</b>	1.74e-3	<b>1.15e-4</b>	2.59e-4
150	<b>6.11e-6</b>	1.15e-3	5.26e-5	1.51e-4
200	<b>3.06e-7</b>	1.52e-3	3.37e-5	8.61e-5

Table 1: Projection errors calculated on the test set achieved by the different approaches. We use **bold** to highlight the best values.

Further, we report in Figure 6 the reduction errors achieved by DL-ROM and inv-DL-ROM with and without spectral normalization for different dimension of the trial manifold  $\in \{3, 4, 5, 10, 20\}$  and in Table 2 we report the values. The dimensions of the manifold were chosen to balance reduction capabilities and accuracy of the learned ROMs. By solely replacing the convolutional AE with the inv-AE, the inv-DL-ROM is capable of improving the reduction errors approximately by a factor 2.5.

Manifold Dimension	DL-ROM	Inv-DL-ROM	Inv-DL-ROM (spectral norm.)
3	5.53e-3	<b>2.12e-3</b>	3.04e-3
4	4.96e-3	<b>2.19e-3</b>	3.09e-3
5	4.28e-3	<b>1.99e-3</b>	2.76e-3
10	4.95e-3	<b>1.81e-3</b>	2.31e-3
20	4.51e-3	<b>1.64e-3</b>	2.42e-3

Table 2: Reduction errors calculated on the test set achieved by the different approaches. We use **bold** to highlight the best values.

## 4.2 Flow Around an Obstacle

As a second challenging and high-dimensional test case, we use the fluid flow around an obstacle. Similarly to [48], we consider a 2-dimensional channel of dimension  $[0, 10] \times [0, 2]$  with a circular obstacle placed in  $(1, 1)$  with a radius of 0.2. The obstacle can be deformed along the x-axis on its left and right side by  $\gamma_l \in [0.2, 0.6]$  and  $\gamma_r \in [0.2, 1.0]$ , respectively. We also assume incompressible flow, whose dynamics is described by the unsteady Navier-Stokes

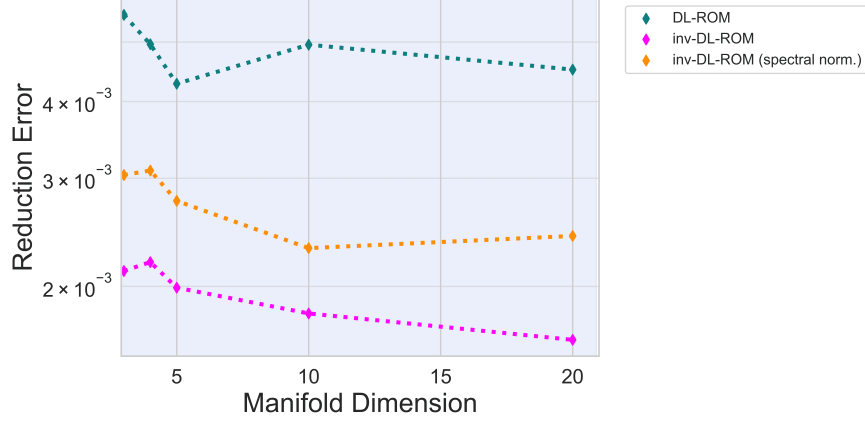


Figure 6: Reduction errors (8) calculated on the test set  $\mathbf{X}_{\text{test}}$  for different dimensions of the trial manifold of DL-ROM and inv-DL-ROM with and without spectral normalization.

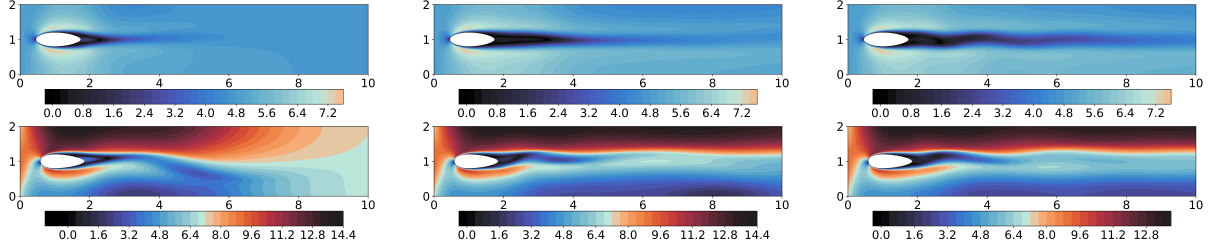


Figure 7: Examples of magnitude of the velocity fields of the flow around an obstacle at different timesteps and parameter instances.

equations

$$\begin{cases}
 \frac{\partial \mathbf{v}(\mathbf{y}, t)}{\partial t} - \nu \Delta \mathbf{v}(\mathbf{y}, t) + (\mathbf{v}(\mathbf{y}, t) \cdot \nabla) \mathbf{v}(\mathbf{y}, t) + \nabla p(\mathbf{y}, t) = 0 & \text{in } \Omega(\boldsymbol{\mu}) \times (t_0, t_f) \\
 \text{div } \mathbf{v}(\mathbf{y}, t) = 0 & \text{in } \Omega(\boldsymbol{\mu}) \times (t_0, t_f) \\
 \mathbf{v}(\mathbf{y}, t) = \mathbf{v}_{\text{in}}(\mathbf{y}, t; \boldsymbol{\mu}) & \text{on } \Gamma_{\text{in}} \times (t_0, t_f) \\
 \mathbf{v}(\mathbf{y}, t) = \mathbf{0} & \text{on } \Gamma_{\text{obs}}(\boldsymbol{\mu}) \times (t_0, t_f) \\
 \mathbf{v}(\mathbf{y}, t) \cdot \mathbf{n}(\mathbf{y}) = 0 & \text{on } \Gamma_{\text{walls}} \times (t_0, t_f) \\
 (\nu \nabla \mathbf{v}(\mathbf{y}, t) - p(\mathbf{x}, t) \mathbf{I}) \mathbf{n}(\mathbf{y}) \cdot \boldsymbol{\tau}(\mathbf{x}) = 0 & \text{on } \Gamma_{\text{walls}} \times (t_0, t_f) \\
 (\nu \nabla \mathbf{v}(\mathbf{y}, t) - p(\mathbf{y}, t) \mathbf{I}) \mathbf{n}(\mathbf{x}) = 0 & \text{on } \Gamma_{\text{out}} \times (t_0, t_f) \\
 \mathbf{v}(\mathbf{y}, 0) = \mathbf{0} & \text{in } \Omega(\boldsymbol{\mu}) \times \{t = t_0\}
 \end{cases} \quad (9)$$

where  $\Omega(\boldsymbol{\mu}) = \Omega(\gamma_l, \gamma_r)$  is the domain of interest depending on the parameters  $\gamma_l$  and  $\gamma_r$ ,  $t_0 = 0$  is the initial time,  $t_f > 0$  is the final time,  $\mathbf{y} = (y_1, y_2)$  indicates the spatial variables,  $\mathbf{v}(\mathbf{y}, t) : \Omega(\gamma_l, \gamma_r) \times [0, t_f] \rightarrow \mathbb{R}^2$  is the velocity,  $p(\mathbf{y}, t) : \Omega(\gamma_l, \gamma_r) \times [0, t_f] \rightarrow \mathbb{R}$  is the pressure,  $\mathbf{v}_{\text{in}}(\mathbf{y}, t; \boldsymbol{\mu}) : \Gamma_{\text{in}} \times [0, t_f] \rightarrow \mathbb{R}^2$  is the time and parameters-dependent inflow datum,  $\nu = 0.01$  is the kinematic viscosity,  $\mathbf{n}(\mathbf{y})$  and  $\boldsymbol{\tau}(\mathbf{y})$  are the normal and tangential tensors. The fluid starts with zero velocity at  $t_0 = 0$  and enters the domain from the left boundary with intensity  $\gamma_{\text{in}} \in [1.0, 10.0]$  and angle of attack  $\alpha_{\text{in}} \in [-1.0, 1.0]$  as defined in

$$\mathbf{v}((0, y_2), t) = (\gamma_{\text{in}} \cos \alpha_{\text{in}}, y_2(2 - y_2) \gamma_{\text{in}} \sin \alpha_{\text{in}}),$$

where the parabolic profile  $y_2(2 - y_2)$  is used to prevent discontinuities as in [48]. We use on a mesh with  $N = 80592$  degrees of freedom for the velocities and solve (9) through the incremental Chorin-Temam projection method for  $t_f = 5\text{s}$ , and  $\Delta t = 0.05\text{s}$  using the finite element solver in `fenics` [49].

Our goal is to recover the velocity field  $\mathbf{v}$  for different values of the parameters  $\boldsymbol{\mu}(\gamma_l, \gamma_r, \gamma_{\text{in}}, \alpha_{\text{in}})$ . The parameter domain is  $\mathcal{P} = [0.2, 0.6] \times [0.2, 1.0] \times [1.0, 10.0] \times [-1.0, 1.0]$ , corresponding to Reynolds numbers in the range  $[40, 1600]$ , where we choose a training set of parameters  $\mathcal{P}_{\text{train}}$  by randomly sampling 80 times from  $\mathcal{P}$ , the validation

set of parameters  $\mathcal{P}_{\text{valid}}$  by randomly sampling 10 times from  $\mathcal{P}$ , and the test set of parameters  $\mathcal{P}_{\text{test}}$  by randomly sampling 10 times from  $\mathcal{P}$ . Therefore, the training set  $X_{\text{train}}$  is composed of the 80 FOM solutions generated for the parameters  $\mathcal{P}_{\text{train}}$ . Further, we keep 10 FOM solutions for the validation set  $X_{\text{valid}}$ , while the test set  $X_{\text{test}}$  is composed of 10 FOM solutions generated with 10 unseen parameter values.

Due to the high dimensionality of the fluid velocities, we first apply the POD to the snapshots to reduce the dimensionality from 80592 to  $r = 512$ , namely 256 dimensions per velocity component, posing a lower bound on the projection error of  $2.6 \times 10^{-3}$ . We compare our inv-AE with and without spectral normalization with the convolutional AE introduced in [5] for a similar test case, where we train the different AE models for 1500 epochs with AdamW optimizer with different manifold dimensions  $\in \{1, 2, 3, 4, 5, 10, 20, 50, 100\}$ . For all the models, we use learning rate equal to  $1e-4$ , weight decay equal to  $1e-4$ , and we employ early stopping if the validation loss does not decrease after 500 epochs of training.

In Figure 8, we show the projection error (7) obtained using the convolutional AE, inv-AE, and inv-AE with spectral normalization, and in Table 1 we report the values. In addition, we report the projection error when truncating the POD to  $r = 512$ . Even in this case, both inv-AE versions reduce the projection error compared to the convolutional AE. Moreover, for both of the inv-AE, we observe a monotone decay of the projection error, which is not the case for the convolutional AE.

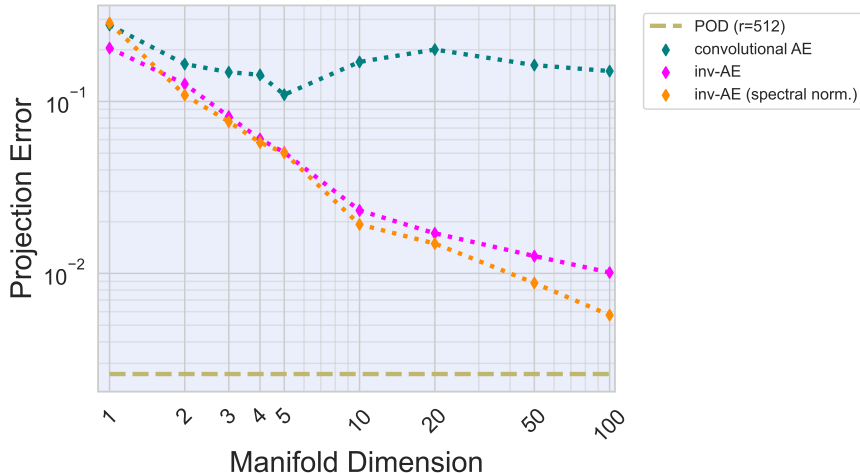


Figure 8: Projection errors (7) for different dimensions of the trial manifold.

Manifold Dimension	Convolutional AE	Inv-AE	Inv-AE (spectral norm.)
1	2.78e-1	<b>2.05e-1</b>	2.86e-1
2	1.65e-1	1.26e-1	<b>1.09e-1</b>
3	1.48e-1	8.16e-2	<b>7.63e-2</b>
4	1.43e-1	6.05e-2	<b>5.77e-2</b>
5	1.09e-1	5.05e-2	<b>5.02e-2</b>
10	1.70e-1	2.33e-2	<b>1.93e-2</b>
20	2.00e-1	1.71e-2	<b>1.49e-2</b>
50	1.63e-1	1.26e-2	<b>8.80e-3</b>
100	1.50e-1	1.01e-2	<b>5.72e-3</b>

Table 3: Projection errors calculated on the test set achieved by the different approaches. We use **bold** to highlight the best values.

Finally, in Figure 9, we show the reduction errors (8) of POD-DL-ROM and the POD-inv-DL-ROMs with and without spectral normalization and in Table 1 we report the values. Even in this case, by simply replacing the convolutional AE with the inv-AE, we are capable of improving the reduction error of the POD-DL-ROM architecture.

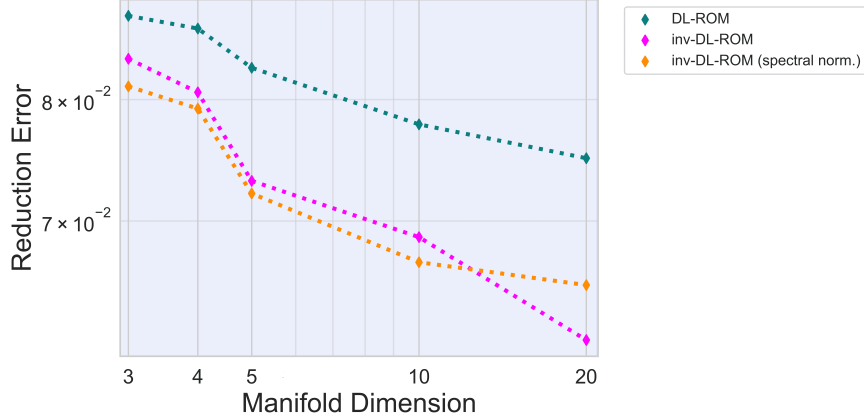


Figure 9: Reduction errors (8) of DL-ROM and inv-DL-ROM.

<b>Manifold Dimension</b>	<b>POD-DL-ROM</b>	<b>POD-Inv-DL-ROM</b>	<b>POD-Inv-DL-ROM (spectral norm.)</b>
1	8.77e-2	8.37e-2	<b>8.12e-2</b>
2	8.65e-2	8.06e-2	<b>7.92e-2</b>
3	8.28e-2	7.32e-2	<b>7.22e-2</b>
4	7.78e-2	6.88e-2	<b>6.69e-2</b>
5	7.50e-2	<b>6.14e-2</b>	6.52e-2

Table 4: Reduction errors calculated on the test set achieved by the different approaches. We use **bold** to highlight the best values.

## 5 Conclusion

In this work, we propose an invertible AE architecture, named inv-AE, that allows for solving challenging dimensionality reduction problems. Inv-AE relies on (i) an invertible neural network to effectively learn an analytically invertible encoder-decoder scheme, on (ii) affine coupling layers to ensure numerical stability, and (iii) parameter sharing between encoder and decoder to reduce the number of learnable parameters. Moreover, we propose an integration of the inv-AE with popular data-driven MOR strategies such as DL-ROM and POD-DL-ROM, that we named inv-DL-ROM and POD-inv-DL-ROM.

In numerical experiments dealing with two challenging classes of high-dimensional problems, namely the Burgers’ equation and the flow around an obstacle, we show that inv-AE is capable of achieving a lower projection error than traditional convolutional AE, and that its use in inv-DL-ROM and POD-inv-DL-ROM is beneficial for improving the reduction error of DL-ROM and POD-DL-ROM relying on convolutional AEs. Throughout our results, we show that inv-AE can mitigate the projection-error plateau of traditional AEs architectures and the quality of its reconstruction gradually improves with the increment of the manifold dimension.

While the inv-AE is analytically invertible by construction, the choice of the affine coupling layers is critical for its numerical invertibility. Affine coupling layers are not prone to training instabilities due to the explosion of the Lipschitz constants and the use of spectral normalization (see Appendix A) appears to be only mildly beneficial in combination with POD. Future research will investigate these properties of the inv-AE to derive theoretical results and bounds for the proposed architectures.

## Acknowledgements

NB acknowledges the Project “Reduced Order Modeling and Deep Learning for the real-time approximation of PDEs (DREAM)” (Starting Grant No. FIS00003154), funded by the Italian Science Fund (FIS) - Ministero dell’Università e della Ricerca.

## References

- [1] Alfio Quarteroni, Andrea Manzoni, and Federico Negri. *Reduced basis methods for partial differential equations: an introduction*, volume 92. Springer, 2015.
- [2] Peter Benner, Serkan Gugercin, and Karen Willcox. A survey of projection-based model reduction methods for parametric dynamical systems. *SIAM review*, 57(4):483–531, 2015.
- [3] Jan S Hesthaven, Gianluigi Rozza, and Benjamin Stamm. *Certified reduced basis methods for parametrized partial differential equations*, volume 590. Springer, 2016.
- [4] Peter Benner, Mario Ohlberger, Albert Cohen, and Karen Willcox. *Model reduction and approximation: theory and algorithms*. SIAM, 2017.
- [5] Stefania Fresca, Luca Dede’, and Andrea Manzoni. A comprehensive deep learning-based approach to reduced order modeling of nonlinear time-dependent parametrized PDEs. *Journal of Scientific Computing*, 87:1–36, 2021.
- [6] Ian Goodfellow, Yoshua Bengio, and Aaron Courville. *Deep learning*. MIT press, 2016.
- [7] M. Ohlberger and S. Rave. Reduced basis methods: Success, limitations and future challenges. *Proceedings of the Conference Algoritmy*, pages 1–12, 2016.
- [8] Kathleen Champion, Bethany Lusch, J Nathan Kutz, and Steven L Brunton. Data-driven discovery of coordinates and governing equations. *Proceedings of the National Academy of Sciences*, 116(45):22445–22451, 2019.
- [9] Romit Maulik, Bethany Lusch, and Prasanna Balaprakash. Reduced-order modeling of advection-dominated systems with recurrent neural networks and convolutional autoencoders. *Physics of Fluids*, 33(3), 2021.
- [10] Kai Fukami, Takaaki Murata, Kai Zhang, and Koji Fukagata. Sparse identification of nonlinear dynamics with low-dimensionalized flow representations. *Journal of Fluid Mechanics*, 926:A10, 2021.
- [11] Joseph Bakarji, Kathleen Champion, J Nathan Kutz, and Steven L Brunton. Discovering governing equations from partial measurements with deep delay autoencoders. *Proceedings of the Royal Society A*, 479(2276):20230422, 2023.
- [12] Nicola Rares Franco, Daniel Fraulin, Andrea Manzoni, and Paolo Zunino. On the latent dimension of deep autoencoders for reduced order modeling of PDEs parametrized by random fields. *Advances in Computational Mathematics*, 50(5):96, 2024.
- [13] Kookjin Lee and Kevin T Carlberg. Model reduction of dynamical systems on nonlinear manifolds using deep convolutional autoencoders. *Journal of Computational Physics*, 404:108973, 2020.
- [14] Youngkyu Kim, Youngsoo Choi, David Widemann, and Tarek Zohdi. A fast and accurate physics-informed neural network reduced order model with shallow masked autoencoder. *Journal of Computational Physics*, 451:110841, 2022.
- [15] Patrick Buchfink, Silke Glas, and Bernard Haasdonk. Symplectic model reduction of Hamiltonian systems on nonlinear manifolds and approximation with weakly symplectic autoencoder. *SIAM Journal on Scientific Computing*, 45(2):A289–A311, 2023.
- [16] The-Gia Leo Nguyen, Lynton Ardizzone, and Ullrich Köthe. Training invertible neural networks as autoencoders. In *German Conference on Pattern Recognition*, pages 442–455. Springer, 2019.
- [17] Samuel E Otto, Gregory R Macchio, and Clarence W Rowley. Learning nonlinear projections for reduced-order modeling of dynamical systems using constrained autoencoders. *Chaos: An Interdisciplinary Journal of Nonlinear Science*, 33(11), 2023.
- [18] Simone Brivio and Nicola Rares Franco. Deep symmetric autoencoders from the Eckart-Young-Schmidt perspective. *arXiv preprint arXiv:2506.11641*, 2025.
- [19] Laurent Dinh, David Krueger, and Yoshua Bengio. Nice: Non-linear independent components estimation. *arXiv preprint arXiv:1410.8516*, 2014.
- [20] Laurent Dinh, Jascha Sohl-Dickstein, and Samy Bengio. Density estimation using real NVP. In *International Conference on Learning Representations*, 2017.
- [21] Aidan N Gomez, Mengye Ren, Raquel Urtasun, and Roger B Grosse. The reversible residual network: Backpropagation without storing activations. *Advances in neural information processing systems*, 30, 2017.
- [22] Jens Behrmann, Will Grathwohl, Ricky TQ Chen, David Duvenaud, and Jörn-Henrik Jacobsen. Invertible residual networks. In *International conference on machine learning*, pages 573–582. PMLR, 2019.
- [23] Jörn-Henrik Jacobsen, Arnold Smeulders, and Edouard Oyallon. i-RevNet: Deep invertible networks. In *ICLR 2018-International Conference on Learning Representations*, 2018.

- [24] Durk P Kingma and Prafulla Dhariwal. Glow: Generative flow with invertible 1x1 convolutions. *Advances in neural information processing systems*, 31, 2018.
- [25] Danilo Rezende and Shakir Mohamed. Variational inference with normalizing flows. In *International conference on machine learning*, pages 1530–1538. PMLR, 2015.
- [26] Aditya Grover, Manik Dhar, and Stefano Ermon. Flow-gan: Combining maximum likelihood and adversarial learning in generative models. In *Proceedings of the AAAI conference on artificial intelligence*, volume 32, 2018.
- [27] Will Grathwohl, Ricky TQ Chen, Jesse Bettencourt, Ilya Sutskever, and David Duvenaud. FFJORD: Free-form continuous dynamics for scalable reversible generative models. In *International Conference on Learning Representations*, 2018.
- [28] Ricky TQ Chen, Jens Behrmann, David K Duvenaud, and Jörn-Henrik Jacobsen. Residual flows for invertible generative modeling. *Advances in Neural Information Processing Systems*, 32, 2019.
- [29] Lynton Ardizzone, Carsten Lüth, Jakob Kruse, Carsten Rother, and Ullrich Köthe. Guided image generation with conditional invertible neural networks. *arXiv preprint arXiv:1907.02392*, 2019.
- [30] Lynton Ardizzone, Jakob Kruse, Carsten Rother, and Ullrich Köthe. Analyzing inverse problems with invertible neural networks. In *International Conference on Learning Representations*, 2019.
- [31] Andrew Glaws, Ryan N King, Ganesh Vijayakumar, and Shreyas Ananthan. Invertible neural networks for airfoil design. *AIAA journal*, 60(5):3035–3047, 2022.
- [32] Jens Behrmann, Sören Dittmer, Pascal Fernsel, and Peter Maaß. Analysis of invariance and robustness via invertibility of relu-networks. *arXiv preprint arXiv:1806.09730*, 2018.
- [33] Justin Gilmer, Luke Metz, Fartash Faghri, Samuel S Schoenholz, Maithra Raghu, Martin Wattenberg, and Ian Goodfellow. Adversarial spheres. *arXiv preprint arXiv:1801.02774*, 2018.
- [34] Joern-Henrik Jacobsen, Jens Behrmann, Richard Zemel, and Matthias Bethge. Excessive invariance causes adversarial vulnerability. In *International Conference on Learning Representations*, 2019.
- [35] Jens Behrmann, Paul Vicol, Kuan-Chieh Wang, Roger Grosse, and Jörn-Henrik Jacobsen. Understanding and mitigating exploding inverses in invertible neural networks. In *International Conference on Artificial Intelligence and Statistics*, pages 1792–1800. PMLR, 2021.
- [36] Yunfei Teng and Anna Choromanska. Invertible autoencoder for domain adaptation. *Computation*, 7(2):20, 2019.
- [37] Siyuan Li, Haitao Lin, Zelin Zang, Lirong Wu, Jun Xia, and Stan Z Li. Invertible manifold learning for dimension reduction. In *Machine Learning and Knowledge Discovery in Databases. Research Track: European Conference, ECML PKDD 2021, Bilbao, Spain, September 13–17, 2021, Proceedings, Part III 21*, pages 713–728. Springer, 2021.
- [38] Takeru Miyato, Toshiaki Kataoka, Masanori Koyama, and Yuichi Yoshida. Spectral normalization for generative adversarial networks. In *International Conference on Learning Representations*, 2018.
- [39] Durk P Kingma, Tim Salimans, Rafal Jozefowicz, Xi Chen, Ilya Sutskever, and Max Welling. Improved variational inference with inverse autoregressive flow. *Advances in neural information processing systems*, 29, 2016.
- [40] Stefania Fresca and Andrea Manzoni. POD-DL-ROM: Enhancing deep learning-based reduced order models for nonlinear parametrized PDEs by proper orthogonal decomposition. *Computer Methods in Applied Mechanics and Engineering*, 388:114181, 2022.
- [41] Patrick Buchfink, Silke Glas, Bernard Haasdonk, and Benjamin Unger. Model reduction on manifolds: a differential geometric framework. *Physica D: Nonlinear Phenomena*, 468:134299, 2024.
- [42] Yvon Maday, Anthony T. Patera, and Gabriel Turinici. A priori convergence theory for reduced-basis approximations of single-parameter elliptic partial differential equations. *SIAM Journal on Scientific Computing*, 17(1):437–446, 2002.
- [43] Haasdonk, Bernard. Convergence rates of the POD–greedy method. *ESAIM: M2AN*, 47(3):859–873, 2013.
- [44] Geoffrey E Hinton and Richard Zemel. Autoencoders, minimum description length and Helmholtz free energy. *Advances in neural information processing systems*, 6, 1993.
- [45] Albert Cohen, Charbel Farhat, Yvon Maday, and Agustin Somacal. Nonlinear compressive reduced basis approximation for PDE’s. *Comptes Rendus Mécanique*, 351(S1):357–374, 2023.
- [46] Patrick Buchfink, Silke Glas, and Bernard Haasdonk. Approximation bounds for model reduction on polynomially mapped manifolds. *Comptes Rendues. Mathématique*, 362:1881–1891, 2024.

- [47] Ilya Loshchilov and Frank Hutter. Decoupled weight decay regularization. In *International Conference on Learning Representations*, 2019.
- [48] Matteo Tomasetto, Jan P Williams, Francesco Braghin, Andrea Manzoni, and J Nathan Kutz. Reduced order modeling with shallow recurrent decoder networks. *Nature Communications*, 16(1):10260, 2025.
- [49] Martin Alnæs, Jan Blechta, Johan Hake, August Johansson, Benjamin Kehlet, Anders Logg, Chris Richardson, Johannes Ring, Marie E Rognes, and Garth N Wells. The FEniCS project version 1.5. *Archive of numerical software*, 3(100), 2015.
- [50] Ian Goodfellow, Jean Pouget-Abadie, Mehdi Mirza, Bing Xu, David Warde-Farley, Sherjil Ozair, Aaron Courville, and Yoshua Bengio. Generative adversarial networks. *Communications of the ACM*, 63(11):139–144, 2020.

## A Spectral Normalization

The training stability of NNs is heavily affected by the Lipschitz constant of networks themselves. Therefore, controlling the Lipschitz constant and preventing its rapid growth is crucial from avoiding exploding gradients and for the loss convergence. Spectral normalization [38] is a type of weight normalization that can improve performance of the NN architectures suffering from training instabilities, such as generative adversarial networks [50].

Given a NN layer with weight matrix  $W$ , the spectral norm of  $W$  equals the largest singular value  $\sigma_{\max}(W)$ , i.e.,  $\sigma_{\max}(W) = \|W\|_2$ . Spectral normalization then uses the spectral norm of  $W$  for normalization such that  $\sigma(W) = 1$ , i.e.,

$$W_{\text{SN}} = \frac{W}{\sigma_{\max}(W)},$$

where  $W_{\text{SN}}$  is the spectrally normalized weight matrix.

If the activation functions have Lipschitz constant equal to 1,<sup>2</sup> the Lipschitz constant of a NN can be bounded from about by the product of the spectral norms of the the weight matrices of each layer  $l$

$$L \leq \prod_{l=1}^{N_L} \sigma_{\max}(W^l), \tag{10}$$

where  $N_L$  indicates the number of layers of the network and  $W^l$  the weight matrix associated with  $l^{\text{th}}$  layer. Therefore, if all layers of the network are spectrally normalized, then the Lipschitz constant of the network is bounded from above by 1.

---

<sup>2</sup>This is the case for many activation functions such as ReLU and leaky ReLU.